



Design and calibration of 3D printed soft deformation sensors for soft actuator control[☆]

Qinglei Ji^{a,b}, **Jakob Jansson**^b, **Mikael Sjöberg**^b, **Xi Vincent Wang**^a, **Lihui Wang**^a, **Lei Feng**^{b,*}

^a Department of Production Engineering, KTH Royal Institute of Technology, Stockholm 10044, Sweden

^b Department of Machine Design, KTH Royal Institute of Technology, Stockholm 10044, Sweden

ARTICLE INFO

Keywords:

Closed loop control

Soft actuator

3D printing

Soft sensors

ABSTRACT

Soft actuators made from compliant materials are superior to conventional rigid robots in terms of flexibility, adaptability and safety. However, an inherent drawback of soft actuator is the low actuation precision. Implementing closed loop control is a possible solution, but the soft actuator shape can hardly be measured directly by commercially available sensors, which either are too stiff for integration or cause performance degradation of the actuator. Although 3D printing has been applied to print bendable sensors from conductive materials, they either have larger stiffness than the soft actuator or are made from specially designed materials that are difficult to reproduce. In this study, easily accessible commercial soft conductive material is applied to directly 3D print soft sensors on soft actuators. Different configurations of the printed sensors are studied to investigate how the sensor design affects the performance. The best sensor configuration is selected to provide shape feedback using its changing resistance during deformation. Compared with a commercial flexible bending sensor, the printed sensor has less influences on the soft actuator performance and enjoys higher shape estimation accuracy. Closed loop shape control of the actuator using feedback from the 3D printed sensor is then designed, implemented and compared with the control results using image feedback. A gripper consisting of three individually controlled soft actuators demonstrates the applications of the soft sensor.

1. Introduction

Soft actuators are built with highly flexible materials and can perform tasks that request compliance and adaptability from the robot [1, 2]. The robots whose whole bodies or the actuators are soft are often called soft robots. The development of soft actuators and soft robots has been fast in both academic and industry communities. The broad applications of soft robots include medical treatment [3,4], products gripping [5] and objects transportation [6,7]. Despite above achievements, the wide application of soft actuators is still hindered by inherent limitations. The biggest drawback of soft actuators is the poor precision. Compared with rigid robots using motors and rigid connections, the flexible bodies of the soft actuators also result in larger difficulties in precisely controlled operations.

To address this problem, force- and shape-feedback control of the soft actuator is applied in prior studies [8]. Gerboni et al. [9] integrate commercially available flex bend sensors to the Flexible fluid actuators (FFAs) which use fluid pressure to produce high deformation. The feedback signal from the bending sensor is then used to regulate the shape of the actuator. Cao et al. [10] develop a bioinspired adaptive

controller to perform shape feedback control of dielectric elastomer actuators (DEAs), which can produce large strains with electric stimuli. The bioinspired adaptive controller has a neural network-like structure to approximate a non-linear controller. When a DEA is actuated, its capacitance changes and the signal is used as the feedback for the controller. Tawk et al. [11] integrate soft pneumatic sensing chambers in a 3D printed soft finger and use the volume changes in the chambers to predict the bending angles and touch forces of the finger. Sonat et al. [12] develop and embed soft strain sensors onto the soft pneumatic actuators and perform closed loop haptic force control.

However, the aforementioned examples either require complex fabrication processes of the soft actuators or need extra effort to integrate shape or force feedback sensors for the closed loop control. Recently, researchers in the 3D printing (3DP) community try to 3D print the soft actuators directly using soft materials and integrate or print the feedback sensors during the 3D printing process, which largely reduces human labor in the fabrication process and increases the integration of the soft actuators with feedback sensors [13,14]. Truby et al. [15] print soft somatosensitive actuators that can enable simultaneous haptic,

[☆] This paper was recommended for publication by Associate Editor Gianluca Palli.

* Corresponding author.

E-mail address: lfeng@kth.se (L. Feng).

proprioceptive, and thermoceptive sensing using ionically conductive gels. Elgeneidy et al. [16] print flexible strain sensors using conductive Polylactic Acid (PLA) filaments. Since the sensor is a thin sheet, it can be bent to some extent even though the base material is rigid. The conductivity of the printed sensors changes when deformed. Similarly, Hainsworth et al. [17] also use doped PLA for the 3D printing of integrated strain sensors for soft actuators. Obvious resistance change is observed during actuator deformation. Yang et al. [18] design new shapes of pressure and position sensors that are made of conductive elastomers (mixture of Thermoplastic Polyurethane (TPU) and Carbon Black) with piezoresistive effect. The pressure sensors are placed in each segment of the soft actuators to provide the local pressure monitoring and position sensors are placed between the segments to provide bending feedback. Tawk et al. [19] discuss the latest advances in 3D printed actuators and sensors in a more recent review work.

As a short summary, the existing studies use either self-developed materials or customized designs to fabricate the sensors applicable for the soft actuators. These sensors either have limited sensing ranges or are restricted to application scenarios. Furthermore, the preparation of the self-developed materials also require expert operation which hinders the wide application of these approaches. 3D printable soft sensors featured with easy-preparation, high accuracy and free-form design are required.

In our prior work [1], a 3D printed bellow type soft actuator is developed and image feedback that acquires the real time bending angle of the actuator is applied for the shape control. However, The method is limited to single actuator control because multiple actuators will intersect with each other in the image sequence and cause unpredictable feedback noise. To address this issue and the previously mentioned problems, this study designs and fabricates a strain sensor that can be directly 3D printed using a flexible conductive filament. The filament is commercially available and has excellent printability. The printed material is strain-sensitive and can hence be used for strain sensors. Different shape configurations of the printed sensors are investigated regarding the resistance-deformation relationship, the drifting and the hysteresis. A sensor that performs well in terms of the three criteria are selected to be integrated with soft actuators to provide shape feedback. To exhibit the advantages of the printed sensor, a commonly used flexible bending sensor is also integrated on the soft actuator for a comparative study. The printed sensor has less interference on the flexible deformation of the soft actuator and provides better shape estimation accuracy.

The printed sensor is then used to build a shape regulation controller for the soft actuator. The control algorithm is developed by pole-placement and the dynamic model of the soft actuator obtained by model identification with experiment data. The precision of the controlled soft actuator is quantified by experiments. Despite sensing errors caused by the printed sensor, the accuracy of the controlled soft actuator still meets design requirements. For the case study, a gripper of three such actuators is fabricated as shown in Fig. 12. The gripper is applied for grasping tasks such as holding a wet sponge without water leakage and do some simple drawings with a painting brush.

The paper is organized as follows: Section 2.1 introduces the 3D printing and integration process of the soft actuator and the soft sensor. Section 2.2 depicts the experimental setup for characterizing the sensor performance and performing closed loop control. Section 3 introduces the evaluation and selection of the soft sensor. Section 4.1 introduces the modeling of the soft actuator. Section 4.2 shows the advantages of the printed soft sensor over a commercial flexible sensor, and develops the closed loop control based on the sensor feedback. Section 5 introduces the case study of a controlled soft gripper using previous studies and Section 6 concludes the paper.

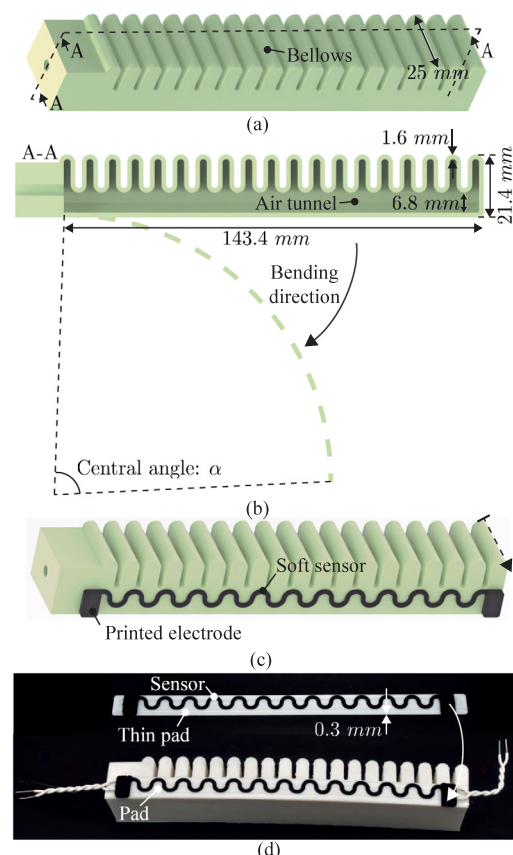


Fig. 1. Soft actuator. (a) Soft actuator schematic. (b) Cross-section A-A. (c) Soft actuator with integrated soft sensor. (d) 3D printed soft actuator with sensors printed on pad structure.

2. 3DP and experiments of soft actuators and sensors

2.1. Multi-material 3D printing of soft actuators and sensors

The soft actuator is bellows type as shown in Fig. 1(a) and is fully composed of flexible materials. The asymmetric structure enables the actuator to bend towards one direction when the actuator is pressurized. The bellows side inflates more and thus the actuator bends to the other direction. Fig. 1(b) shows the cross-section A-A and the detailed dimensions of the actuator. In ideal deformation, the deformed actuator forms an arc shape and the central angle of the arc is used to present the deformation of the actuator. Note that when the actuator is deformed for some cycles, the central angle cannot recover to zero due to residual force. In this study, the unrecoverable residual central angle is $\alpha_{res} = 30^\circ$. For clarity, in the following text, the central angle is defined as the difference between the real central angle α_{real} and the residual central angle α_{res} as $\alpha = \alpha_{real} - \alpha_{res}$.

Fig. 1(c) shows an example of the actuator integrated with a soft sensor. The sensor is a long twisting strip and distributes along the soft actuator on the external side of the wide air tunnel. The sensor is also flexible so that it can bend with the actuator without interference with its nature bending. The sensor has two electrodes on both sides for connecting electrical wires.

To fabricate the above integrated actuator and sensor, a TL-D3 Pro Dual Extruder Deposition Modeling (FDM) 3D Printer is used. It has two independent direct drive extruders that can extrude flexible materials smoothly. The soft actuator body and the sensor are printed with the two extruders with two different materials respectively. The actuator body is 3D printed using NinjaFlex 3D printing filament, which is

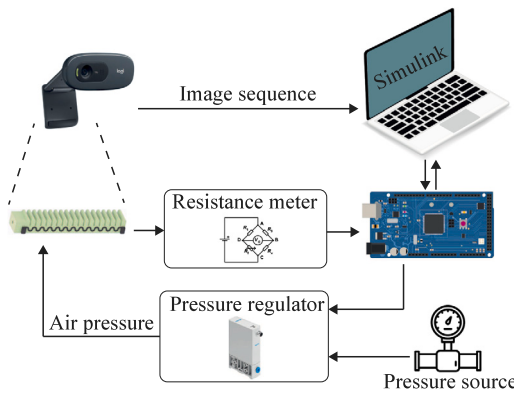


Fig. 2. Experimental setup for the closed loop control of soft actuator with printed sensor.

Thermoplastic polyurethane (TPU) and has a shore hardness of 85 A and tensile modulus of 12 MPa. The material can stand elongation up to 660% [20]. The EEL 3D printer filament is used as the printing material for the sensors. The EEL is conductive TPU which is a mixture of TPU and carbon black. Its electric resistance is deformation-responsive due to the changed distribution of carbon black during deformation. The material is also flexible with tensile stress of 11 MPa at 300% elongation and can be elongated up to 355%. The sensor is directly printed on to the already printed actuator. The 3DP parameters can be found in our prior reports [21]. After the printing is finished, a 4 mm outer diameter Polytetrafluoroethylene (PTFE) tube for pressure supply is inserted into the predesigned hole on the soft actuator for intaking air pressure and sealed with Epoxy adhesive (Loctite EA 3430) [1]. The printing of the soft actuator without the sensor takes around 13 hours and is time-consuming. To save the experiment time, in the sensor testing stage described in later sections, different sensors are directly 3D printed on a thin pad of 0.3 mm and the pad is then glued to the actuator body using a thin layer of superglue from Loctite as shown in Fig. 1(d). The 3DP process of the sensor with pad and the gluing process take around 20 minutes. The glued parts can easily be separated and the actuator body can then be reused to greatly reduce the experiment time. After each actuator and sensor being printed, they are post-processed by applying a sine wave air pressure with an amplitude of 4 bars on the soft actuator for 50 cycles of deformation to stabilize the actuator and sensor performance.

2.2. Test rig for the soft sensor

To provide the best feedback signal, the performance of different sensor designs is tested using the test rig in Fig. 2. A Logitech c270 web camera is used to capture the deformation of the actuator in real time. Three colorful reference points are marked on the soft actuator to present the actuator shape [1]. These coordinates of the recognized markers are used to derive the central angle of the bent soft actuator. The image feedback module is only applied in the testing stage for calibration and analysis. It is not needed after the sensor is well calibrated for the soft actuator.

The computer is also connected with an Arduino Mega 2560 microcontroller board via serial communication. A MATLAB Simulink program runs on the computer and downloads the compiled program to the microcontroller board and also communicates with the board in real time to monitor the system status and send commands to the board. A proportional pressure regulator (Festo VEAB-L-26-D9-Q4-V1-1R1) is connected with the microcontroller board and is supplied with a pressure source of 6 bars. The pressure regulator receives analogue voltage between 0 V and 10 V from the microcontroller board and regulates the pressure output between 0% and 100% of the pressure

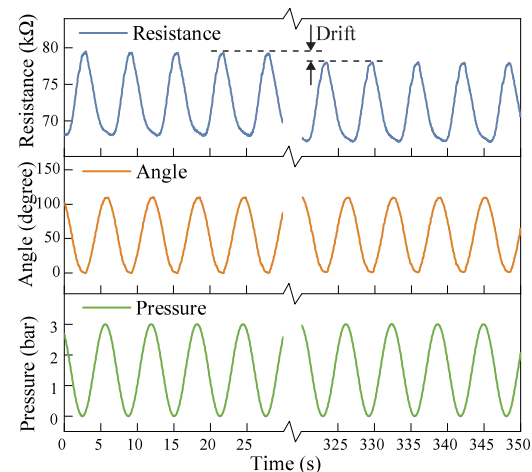


Fig. 3. Actuator angle and sensor resistance responses with a sine wave pressure input.

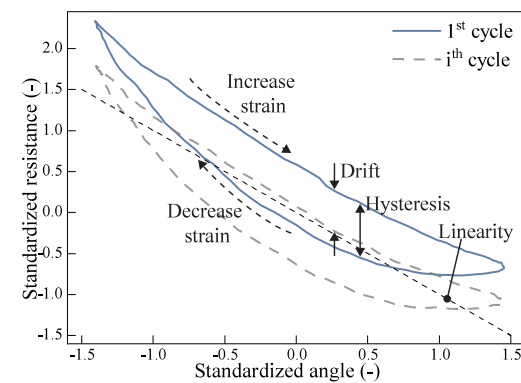


Fig. 4. Illustration of the hysteresis, linearity error and drifting of the soft sensor undertook cycled bending deformation.

source accordingly. The pressure outputs from the pressure regulator are verified with a pressure sensor (Festo SPAU-P6R-W-Q4D-L-PNLK-PNVBA-M12U) before the experiments. The pressure is then supplied directly to the actuator with a 4 mm outer diameter Polytetrafluoroethylene (PTFE) tube. A resistance meter circuit using Wheatstone bridge is designed and fabricated which connects the sensor on the soft actuator and converts the varied electric resistance of the sensor to analogue signals between 0 V and 5 V. The analogue signals are then measured by the microcontroller board as digital readings between 0 and 1023.

3. Optimal design and model of the soft sensor

3.1. Resistance-deformation relationship of the sensor

The electric resistance of the printed sensor changes when the sensor is deformed. Fig. 3 shows an example of the angle variation and the sensor resistance changing when a sine wave form pressure input is applied to the actuator shown in Fig. 1(d). The angle variation follows the trend of the pressure while the resistance value changes reversely, i.e., the resistance decreases when the deformation angle increases and vice versa. The resistance curve also follows the shape of a sine wave with the same frequency as the pressure input and the angle variation. Thus it is possible to use the real time resistance value of the sensor to estimate the deformation of the sensor. It is also observed that when the pressure loading is repeated for multiple times, there is a drift of the overall electric resistance values for the same deformation level as marked in Fig. 3. The drift can decrease the estimation accuracy in the long term.

For the convenience of data analysis, the sensor resistance R and angle α variation data from a certain number of deformation cycles are standardized as follows:

$$\hat{R} = \frac{R - \bar{R}}{\sigma_R} \quad (1)$$

$$\hat{\alpha} = \frac{\alpha - \bar{\alpha}}{\sigma_\alpha} \quad (2)$$

where \hat{R} , $\hat{\alpha}$ are the standardized resistance and angle. \bar{R} and $\bar{\alpha}$ are the average resistance and average angle values of the repeated deformation cycles. σ_R and σ_α are the standard deviation of the resistance and angle values from the repeated deformation cycles. Therefore, the standardized resistance \hat{R} and standardized angle $\hat{\alpha}$ both have a mean of 0 and standard deviation of 1. In our study, the data from $N = 100$ cycles of deformation are used for the standardization.

Fig. 4 shows the standardized resistance change versus the standardized angle change for the first and the i^{th} ($1 < i \leq N$) loading cycles from the record shown in **Fig. 3**. The solid blue line illustrates the resistance change process of the first cycle. Obviously, the relationship between the angle and the resistance varies for the angle increasing and decreasing processes. This results in different resistances for the same deformations. The phenomenon is expressed by the maximum difference between the standardized resistances for any standardized angle in one loading cycle, denoted as *hysteresis H*. For the multiple deformation cycles, H is calculated using the average hysteresis of all cycles. In one deformation cycle, the angle increasing process is evenly sampled by M points with indexes from 1 to M . The angle decreasing process is also evenly sampled by M points with indexes from M to $2M - 1$. Thus the sampling points 1 and $2M - 1$ refer to the same angle and the hysteresis H^n for the n^{th} deformation cycle is defined as:

$$H^n = \max_{m=1}^M (\hat{R}_m^n - \hat{R}_{2M-m}^n) \quad (3)$$

The superscript n indicates the n^{th} deformation cycle. For a total number of $N = 100$ cycles, the hysteresis H is defined as

$$H = \frac{1}{N} \sum_{n=1}^N H^n \quad (4)$$

Comparing the curves of the first cycle and the i^{th} cycle in **Fig. 4**, it is observed that the resistances of the i^{th} cycle are offset downwards. This is due to the drifting phenomenon explained in **Fig. 3**. As a result, the resistance is not entirely determined by the deformation angle. The cycles and direction of the deformation also influence the resistance. This variation is noted as the *drifting* issue and is described using the maximum difference of the standardized resistances at the same sampling point $m = (1, \dots, 2M - 1)$:

$$D_m = \max_{n=1}^N \hat{R}_m^n - \min_{n=1}^N \hat{R}_m^n \quad (5)$$

Then the drifting of all data is:

$$D = \max_{m=1}^{2M-1} D_m \quad (6)$$

The relation of the standardized resistance and the standardized deformation angle is then approximated with a linear function. Since both variables are standardized, the fitted linear function always passes the origin as illustrated in **Fig. 4** and can be expressed as:

$$\hat{R} = p\hat{\alpha} \quad (7)$$

where \hat{R} is the standardized resistance of the sensor and $\hat{\alpha}$ is the standardized deformation angle. p is the coefficient to be identified by fitting measurement data. After p is identified, we can estimate the deformation angle from the measured resistance:

$$\hat{\alpha} = \frac{\hat{R}}{p} \quad (8)$$

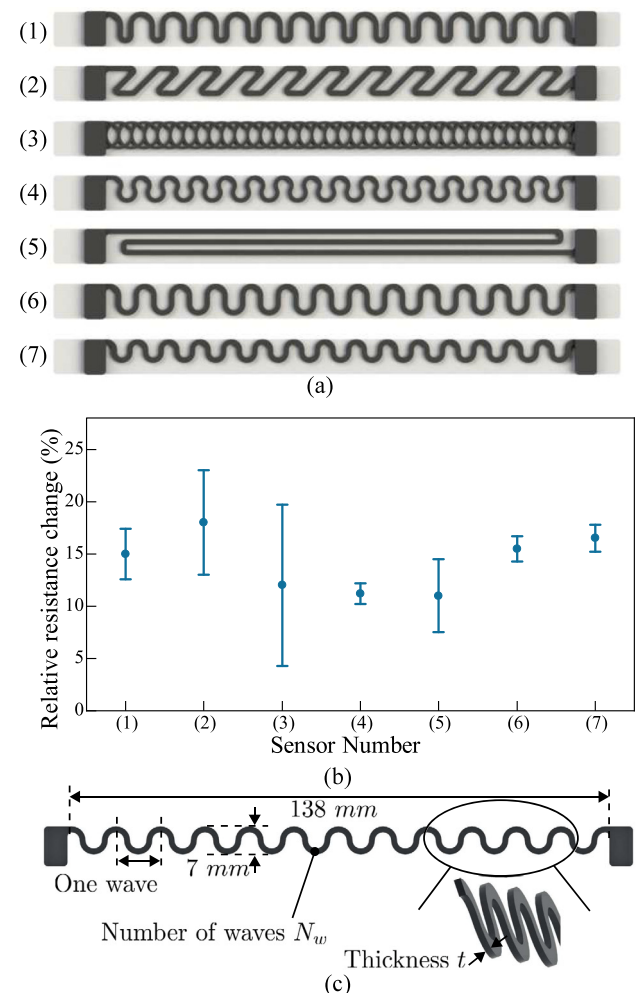


Fig. 5. Sensor shape. (a) Tested wave shape sensors. (b) The relative resistance change of these sensors for the same deformation. (c) Sine wave sensor.

More intuitively, according to (1), (2) and (8), the deformation angle α can be estimated by the sensor resistance R using the following equation:

$$\alpha = \frac{\sigma_\alpha}{p\sigma_R} (R - \bar{R}) + \bar{\alpha} \quad (9)$$

In this study, data of the standardized resistance variation versus the standardized actuator angle of $N = 100$ loading cycles are used to find the linear coefficient p . The average Root Mean Square Error (RMSE) from the linear fitting of all cycles is used to present the *linearity error* of the resistance versus the deformation, denoted as:

$$L = \frac{1}{N} \sum_{n=1}^N \sqrt{\frac{\sum_{m=1}^{2M-1} (\hat{R}_m^n - p\hat{\alpha}_m^n)^2}{2M-1}} \quad (10)$$

where $p\hat{\alpha}$ refers to the estimated standardized resistance and \hat{R} refers to the actual observed value. The above three indices H , D and L are then applied to evaluate the performance of the printed sensors.

3.2. Sensor profiles

The three properties of the sensor are greatly affected by the shape of the sensor. Thus it is important to investigate the best sensor profile for accurate shape feedback. For the selection of the sensor shapes, many sensor shapes are printed and **Fig. 5(a)** illustrates a few promising examples. These sensor shapes are inspired by the commonly applied

wave form strain sensor shapes that have been examined to perform well in many studies [22–24]. Their resistance–deformation performance is then tested and the relative resistance change $\Delta R/R_0$ is calculated from the measurement data, where ΔR is the changed sensor resistance and R_0 is the nominal resistance with no deformation. The relative resistance change of a preferred sensor shape should be both large and stable.

Fig. 5(b) shows the testing results for the tested sensors and each data point refers to the averaged results of ten printed sensors for the corresponding shape. For the deformation, the actuator is loaded with a pressure of 3 bar. **Fig. 5(b)** shows that the two last sine wave shape provides the largest relative resistance change with low variance, indicating better reproducibility than other shapes. It is also observed that sensors with sharp turning edges or many joints, result in large variance in the relative resistance change (for example sensor (2), (3)), probably because these sensors tend to have strain and stress concentration, leading to irregular resistance change. Thus, in this article, we focus on the sine wave form sensor with different wave parameters as shown in **Fig. 5(c)**. Following the dimensions of the soft actuator, the sensor excluding the electrode sides has an overall length of $L_s = 138$ mm and a height of $h_s = 7$ mm.

If the number of total waves is $N_w \in \mathbb{N}^+$, then the wavelength of the sine wave sensor is L_s/N_w . The other parameter describing the sensor shape is the thickness of the sensor t , whose effect on the sensor performance is investigated in [25]. The thickness is adjusted by the number of 3D printed layers. The influence on the sensor performance of these two shape decisive parameters are then investigated.

The number of waves is studied for $N_w \in \{12, 18, 24\}$ and the thickness is studied for $t \in \{0.6 \text{ mm}, 0.9 \text{ mm}, 1.2 \text{ mm}\}$. For a 3DP process with the layer height of 0.3 mm, the number of layers for printing the sensors are 2, 3 and 4 respectively. All combinations of these parameters are then applied and 9 different shape profiles for sensors are tested. At this testing stage, all sensors are printed on the pad and then attached to an actuator as explained in **Fig. 1(d)**. Then the sensors are post-processed using the methods described in Section II.A. For the testing of the sensors, the actuator is applied with a sine signal with an amplitude of 3 bars and a frequency of 1 rad/s, illustrated by **Fig. 3**. The periodical loading is repeated for 100 cycles and the resistance change versus the angle is recorded. The angle and resistance data of the 100 cycles are then standardized to calculate the H , L and D . For each of the nine shape profiles, three sensors with the same profile are printed and tested by applying the above process. Thus for the later analysis of the performance indices H , L , D , a total of 27 sets of measurement data are used.

3.3. Modeling of the sensor performance versus sensor profiles

Denote the values of the three performance parameters as P_H , P_L , and P_D . The relationship between the values of the performance indices P_H , P_L , P_D and the sensor parameters N_w, t needs to be identified. We compare four possible models to express the relation: *linear*, *linear & interaction*, *quadratic*, *quadratic & interaction* and their expressions can be written as follows respectively:

$$P_i = z_i + a_i N_w + b_i t \quad (11)$$

$$P_i = z_i + a_i N_w + b_i t + c_i N_w t \quad (12)$$

$$P_i = z_i + a_i N_w + b_i t + c_i N_w^2 + d_i t^2 \quad (13)$$

$$P_i = z_i + a_i N_w + b_i t + c_i N_w^2 + d_i t^2 + f_i N_w t \quad (14)$$

where $i \in \{H, L, D\}$. For each possible model, z_i , a_i , b_i , c_i , d_i and f_i are the coefficients to be fitted using least squares method for every performance index respectively. The model complexity increases gradually from (11) to (14).

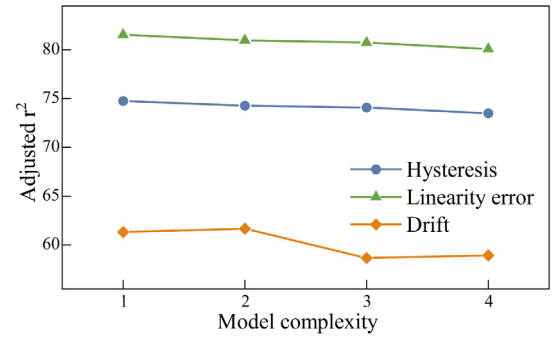


Fig. 6. Fitness of different models in terms of hysteresis, drifting and linearity error.

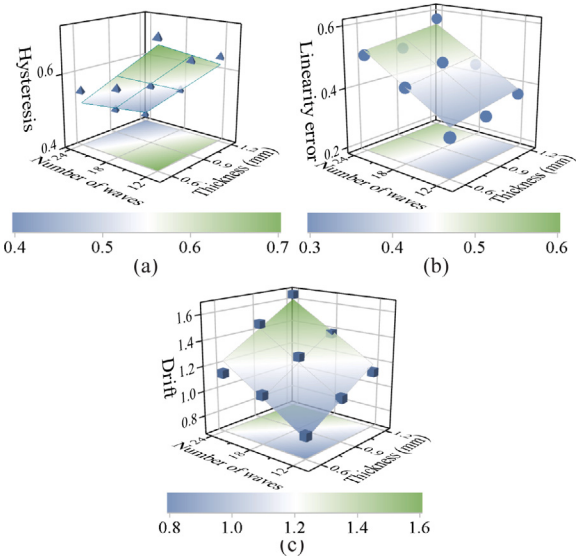


Fig. 7. Sensor performance in terms of (a) hysteresis, (b) linearity error and (c) drifting.

Table 1
Fitted coefficients for the sensor performance indices.

| Coefficients | H | L | D |
|--------------|-----------------------|----------------------|-----------------------|
| z | 9.9×10^{-1} | 1.3×10^{-1} | -3.3×10^{-4} |
| a | -1.5×10^{-1} | 6.5×10^{-2} | 6.3×10^{-1} |
| b | -1.6×10^{-2} | 1.5×10^{-2} | 3.6×10^{-2} |

Our aim is to find the simplest and most accurate model formulated above. **Fig. 6** shows the adjusted r^2 fitness for different models and every point in the figure is calculated by averaging the fitting results from the aforementioned 27 data sets [26]. A larger value of the adjusted r^2 means higher accuracy of the fitting model. The horizontal axis is the model complexity which refers to the models from (11) to (14) respectively. It can be observed that for the hysteresis and linearity error, the simplest linear model has the highest adjusted r^2 fitness and more complex models with higher order items decrease the model fitness. For the drifting, the adjusted r^2 fitness slightly increases when the interaction item is introduced into the linear model. More complex models have lower adjusted r^2 fitness. The trend indicates that the influence of the number of waves N_w and thickness t of the sensor is linear. Considering the results of the three performance indices, the linear model of (11) is selected to describe the influence of sensor shape parameters on the sensor performance. The fitted coefficient values of the linear model for the three performance indices are shown in **Table 1**.

Fig. 7 shows the plots for the three performance indices versus the sensor shape parameters. The fitted functions $P_H(N_w, t)$, $P_L(N_w, t)$,

$P_D(N_w, t)$ are plotted as 3D color-map surfaces. The three performance indexes for each profile are also marked as tetrahedrons, dots and cubes respectively. Fig. 7(a) shows that the hysteresis decreases when the thickness t and number of waves N_w increases. Thus for a smaller hysteresis, larger t and N_w are preferred. Fig. 7(b) shows that the linearity error is better for smaller t and N_w , which is opposite to the hysteresis. The relation between the drifting and t, N_w shows similar trend like the linearity error as shown in Fig. 7(c). Consequently, for the smaller linearity error and drifting, thinner sensors with less number of waves are desired. For the selection of the best sensor parameters, the performance indices are firstly all normalized to 0–1 using their ranges of variation. Then, the three normalized indices are multiplied by three weights of importance w_H, w_L and w_D for the three indices. All weights belong to [0, 1] and their sum is 1. The weighted sum of the three indexes is the overall performance indicator of the sensor profile. In our study, with a balanced consideration of the three performance indices, we define $w_H = 0.4$, $w_L = 0.3$ and $w_D = 0.3$. Thus the optimal sensor that maximizes the overall performance indicator should be thinner with less number of waves and the optimal configurations are:

$$t^* = 0.6 \text{ mm}, N_w^* = 12 \quad (15)$$

The sensor with the optimal profile is used to provide the shape estimation feedback for closed loop control using (9), whose parameters are: $p = -0.9148$, $\sigma_\alpha = 38^\circ$, $\sigma_R = 3.2 \text{ k}\Omega$, $\tilde{\alpha} = 61^\circ$ and $\tilde{R} = 67 \text{ k}\Omega$.

4. Modeling and control of the soft actuator

4.1. Model identification of the soft actuator

To perform closed loop control of the soft actuator, a model is needed to design the closed loop controller. There are several studies addressing the actuator modeling using Finite Element Modeling (FEM) methods [27] or data-driven methods [8,28]. In our prior study [1], we find that a data-driven linear transfer function model is adequate to represent the performance of our 3D printed actuator. The 3D printed soft actuator is applied with a series of air pressures varying from 0.5 bars to 2.25 bars and the central angle responses are recorded from the camera feedback versus the time stamps. The angle response is found to be stable at 1.4 s and the angle at this time stamp is noted as the steady angle. Fig. 8(a) shows the relation between the steady angle α_∞ versus input pressure P and the relation is approximately as linear. The data points are then linearly fitted as shown in the figure. The linear model in Fig. 8(a) can be expressed as $\alpha_\infty = 38P$. The corresponding coefficient of determination r^2 value is 94.7%, which represents that the actuator's static response is close to a linear model and the system steady-state gain is 38. Fig. 8(b) shows the dynamic responses of the step inputs of different pressures. The different responses are then averaged and transfer function models with different orders from 1 to 4 are used to fit the averaged experimental data using *ttest* function in MATLAB. Fig. 8(c) shows the fitness level valued by the coefficient of determination for different model orders. It is observed that increasing the order from 1 to 2 can increase the fitness by around 10%. Increasing the orders above 3 does not improve the fitness significantly. Considering the balance between model accuracy and complexity, the second-order model is selected to represent the dynamics of the soft actuator. The acquired second order discrete time transfer function is:

$$G_p(z) = \frac{B(z)}{A(z)} = \frac{0.9935z + 9.32}{z^2 - 0.9013z + 0.1697} \quad (16)$$

The sampling time is $T_s = 0.05 \text{ s}$ and the corresponding coefficient of determination is $r^2 = 95.2\%$. The model is later used to design the controller.

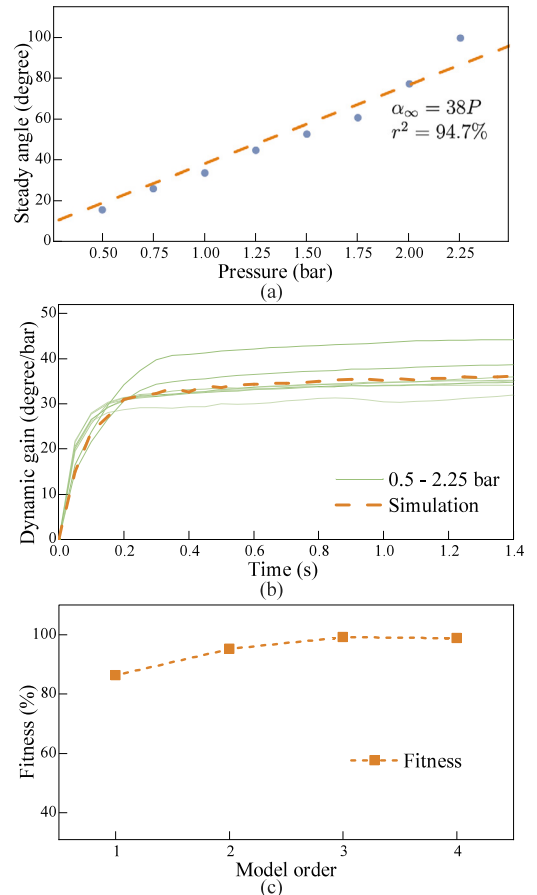


Fig. 8. Model fitting for the soft actuator. (a) Steady angle versus input pressure. (b) Normalized angle variation versus time. (c) Fitness level for different model orders.

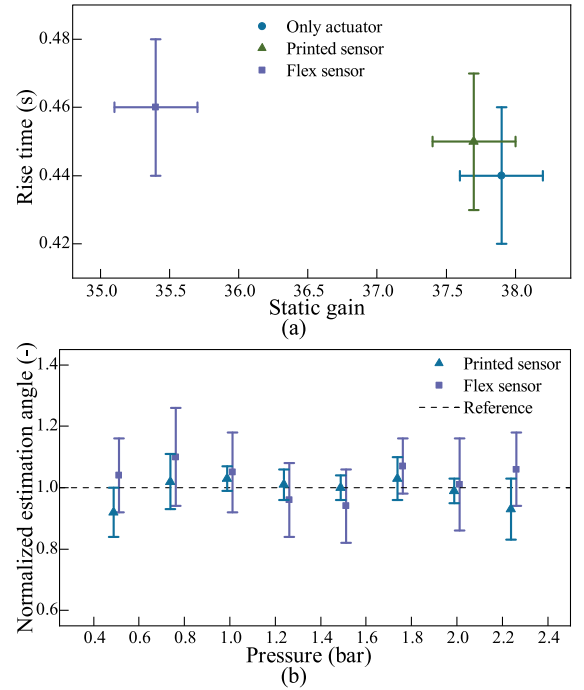


Fig. 9. Comparison of the 3D printed sensor and a commercial Flex sensor. (a) Comparison of the performance of the soft actuator with and without the shape estimation sensors. (b) The estimation errors of the two sensors for different applied pressures on the soft actuator.

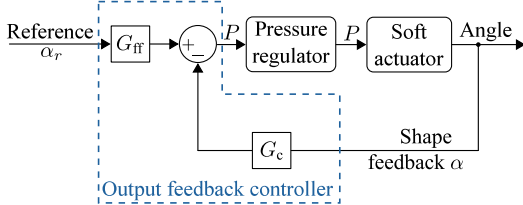


Fig. 10. Closed loop control structure.

4.2. Closed loop control of the soft actuator

Traditional methods integrate commercial flexible bending sensors (noted as Flex sensor) with the soft actuators to acquire the deformed shape. The Flex sensor has different stiffness than the soft actuators and will thus interfere the deformation. On the other hand, the proposed printable soft sensor can estimate the deformation angle of the soft actuator with little interference. As a validation, we compare the influences of using a Flex sensor (SparkFun Flex Sensor 4.5") and the printed sensor on the performances of the soft actuators. The estimation accuracies of the two methods are also compared. The calibration of the Flex sensor is the same as the printed sensor and is thus neglected. Fig. 9(a) shows the rise times and static gains of three cases: the actuator without any sensor, the actuator with the printed sensor, and the actuator with the Flex sensor. Ten tests are performed for each case and the averaged values and the standard deviations are plotted as the data points and the error bars. With the printed sensor, the average static gain of the soft actuator slightly decreases from 37.9 to 37.7 and the average rise time also changes slightly from 0.44 s to 0.45 s. However, with the Flex sensor, the average static gain decreases largely to 35.4 and the average time further increases to 0.46 s. Evidently the Flex sensor has larger influence on the performance of the soft actuator than the printed sensor.

Fig. 9(b) compares the shape estimation accuracy of the two sensors when the soft actuator is driven with different pressures and the camera acquired angle is used as the ground truth. The estimated angles are normalized with the corresponding ground truth for comparison. The printed sensor shows high accuracy with less than 5% estimation error for the pressures from 0.8 bar to 2.0 bar and the error slightly increases for smaller or larger pressures. The Flex sensor has larger average errors when the pressure is between 0.8 bar and 2.0 bar, and the standard deviations of the Flex sensor are generally larger than those of the printed sensor.

The printed sensor is then applied for the closed loop shape control of the soft actuator and the control structure is shown in Fig. 10. The objective of the controller is that the actuation overshoot should also be as small as possible to protect the object which the actuator will touch. Following the control target, the controller requirements are:

- The rise time should be as short as possible.
- The static error is less than 5% of the reference actuation angle.
- Overshoot is less than 5% of the reference actuation angle.

The previous study [1] develops both an error feedback and an output feedback PI controllers to regulate the soft actuator to satisfy the control requirements, but the angle of the actuator is measured by the image feedback module [1]. By contrast, the controller developed in this paper uses the soft sensor to measure the actuator's angle instead of the image feedback module. Even though the soft sensor has larger measurement errors than the image feedback module, our controller can still meet the control requirements with high accuracy.

After systematic comparison, the previous study [1] finds that the output feedback PI controller has shorter response time and higher accuracy. This paper also selects the output feedback PI controller. The

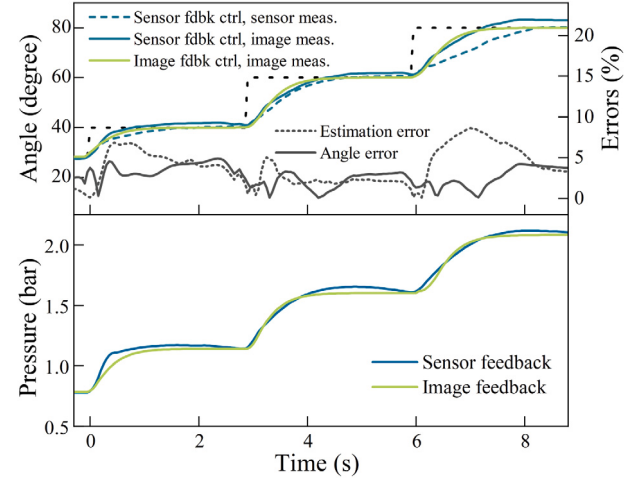


Fig. 11. Closed loop control results comparison with the sensor feedback and the image feedback.

actuator model developed in (16) is used to develop the output feedback controller that satisfies the above requirements. Pole placement methods are used to determine the parameters. The output feedback control law [1,29] can be expressed as:

$$P(z) = G_{ff}\alpha_r - G_c\alpha \quad (17)$$

where $P(z)$ is the pressure reference sent to the pressure regulator. The pressure regulator is assumed to be an ideal regulator and provides pressure output equal to the pressure reference without delay. The output feedback controller selects G_c to achieve the desired closed-loop poles and selects G_{ff} to ensure the actual angle to follow the reference in a short time. The control structure of G_c for the output feedback PI controller with low pass filter can be expressed as:

$$G_c = \frac{S(z)}{R(z)} = \frac{s_2 z^2 + s_1 z + s_0}{(z-1)(z+r_0)} \quad (18)$$

where s_2 , s_1 , s_0 and r_0 are the parameters defining the controller and need to be calculated with assumed poles. The closed loop specifications define the closed loop polynomial $A_{cl}(z) = A_m(z)A_0(z)$, where A_m has the same order as $G_p(z)$ and can be expressed as $A_m = (z-w_1)(z-w_2)$. With four parameters to be decided, A_0 should also be a second order function and can be expressed as $A_0 = (z-w_3)(z-w_4)$. w_1 , w_2 , w_3 and w_4 are the pole positions that determine the characteristics of the closed loop system and need to be fine-tuned with experimental methods. The Diophantine equation [29] can be expressed as:

$$A(z)R(z) + B(z)S(z) = (z-w_1)(z-w_2)(z-w_3)(z-w_4) \quad (19)$$

s_2 , s_1 , s_0 and r_0 are computed by solving the Diophantine equations. For the output feedback controller, the feed forward part G_{ff} can be expressed as:

$$G_{ff} = \frac{T(z)}{R(z)} \quad (20)$$

where $T(z) = t_0 A_0(z)$ and t_0 is defined as $t_0 = \frac{A_m(1)}{B(1)}$ such that the DC gain from the reference to the output is 1.

For the selection of the pole locations of the closed loop system, different s-plane pole locations are picked and then transferred to the z-plane to be tested with the actuator model. The poles are changed from slower locations to faster locations gradually until the fastest closed loop system is achieved while satisfying the control requirements. The selected pole locations at the z-plane for calculating the controller parameters are: $w_1 = w_2 = 0.82$ and $w_3 = w_4 = 0.74$.

To study the influence of the soft sensor on the control performance, we compare the same output feedback PI controller with two ways

Table 2
Control results.

| Feedback | Sensor feedback | Image feedback |
|----------------------|-----------------|----------------|
| Maximum overshoot | 4% | 1% |
| Average rise time | 1.5 s | 1.1 s |
| Average static error | 2.6% | 0.5% |

of measuring the actual angle. One way is to use the image feedback module and the other is to use the proposed soft sensor. The image feedback has higher accuracy and is considered as the ground truth. Hence, the control implementation using the soft sensor for feedback measurement has degraded performance, but our study shows that the implementation with the printed sensor still satisfies the control requirements.

The upper figure in Fig. 11 shows an example of a sequence of angle control to 40°, 60° and 80° using the aforementioned controllers. The black dotted step trajectory shows the reference angles. The two blue lines are for the implementation using the sensor feedback. The dashed blue line shows the angles estimated by the soft sensor and the solid blue line shows the same angles measured by the image feedback module. Owing to the measurement error of the printed sensor, when the sensor measurement is identical to the reference value, the real angle is slightly larger than the reference. The error causes static error of the controller using the printed sensor. The estimation error of the printed sensor is shown by the dotted gray line and degrades the performance of the controller using the soft sensor. Smaller estimation error is achieved for 60° compared with 40° and 80°, because 60° is closer to the average angle used in the standardization process and the printed sensor has better estimation accuracy. Too large or too small control references cause deviations in angle estimation. During a control task, the estimation error increases when the actuator shape changes quickly at the beginning of a step input and becomes smaller when the actuator stabilizes at the reference shape. The overall estimation error is always less than 10% in all tasks, showing the estimation accuracy of the sensor.

The solid green line shows the control results using the image feedback directly for the same controller. Since the image feedback has better accuracy on the angle measurement, the performance of this control implementation is better than the other implementation using the soft sensor. The solid gray line shows the angle error between the two implementations, with the image feedback one as the ground truth. The angle error is always less than 5%, because the feedback controller and dynamics of the soft actuator reduce the measurement error. The blue and green lines in the lower part of the figure show the corresponding control inputs of air pressure inputs.

Table 2 shows the overall performance of the two feedback approaches. The comparisons are based on the accurate angles measured by the camera for both feedback approaches and the values are acquired by averaging the indices from 5 individual experiments. In summary, the measurement error caused by the printed soft sensor decreases the control performance, but the degradation is relatively small.

5. Case studies

A gripper composed of three soft actuators are fabricated for the application. Each actuator can be individually controlled using the closed loop method developed in Section 4.B. Fig. 12 shows the design and assembly of the gripper. As illustrated in Fig. 12(a), each actuator can be installed into the actuator fixer and then be tightened by a screw. The Side actuator fixers have slots for fixing the screw at different positions. As a result, different actuator angles between the two side actuators and the middle actuator can be realized during assembly as illustrated in Fig. 12(b). A tube path is also designed in the top holder for passing the PTFE pressure tubes of the three actuators. To



Fig. 12. Gripper with three closed loop controlled soft actuators. (a) Exploded view of the gripper. (b) Assembled gripper.

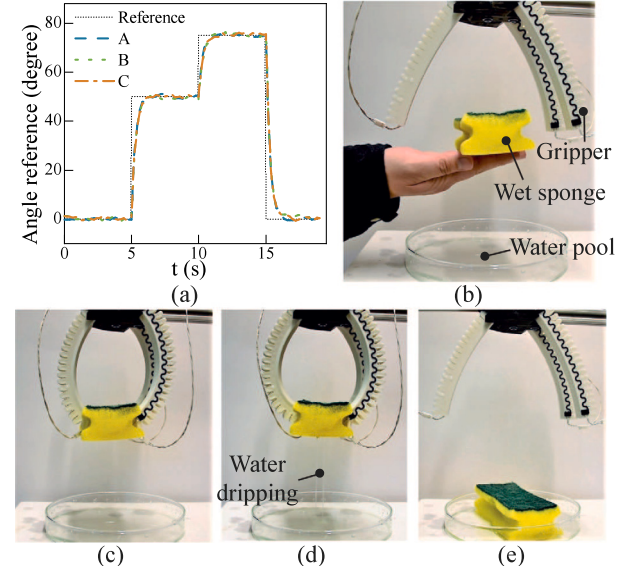


Fig. 13. Grasp a wet sponge. (a) The identical reference angles for the actuator A, B and C and the controlled angles during the grasping of a wet sponge. (b) Gripper is standing by for grasping. (c) Gripper hold the sponge gently with no water leakage. (d) The sponge is squeezed by the gripper and water is pressed out. (e) The sponge is released.

better distinguish the actuators in later studies, the actuators are noted as actuators A, B and C following their positions in the gripper as illustrated in Fig. 12(b).

Two case studies are then tested. The first one applies static shape references to the three actuators for gently grasping a wet soft sponge. The other applies dynamic references to the actuators for moving a painting brush to make drawings. In both cases, the bending references of the actuators are calculated by analyzing the space geometries of the gripper and the objects such that the actuators can gently touch the objects without causing undesired deformation.

5.1. Grasp a wet sponge

The sponge is very soft and easy to be squeezed. When the soft sponge is wet with water or cleanser, it becomes challenging to grasp the sponge without compressing it too much so that the contained water or cleanser is squeezed out. Thus it is vital that the deformation of the gripper is precisely controlled so that the deformation of the soft sponge is acceptable.

Fig. 13 shows the full process of grasping a piece of wet sponge and squeezing the water out at the final steps. Fig. 13(a) shows the changes of angle references for the actuator during the process and the controlled angles. The references for the three actuators A, B and C

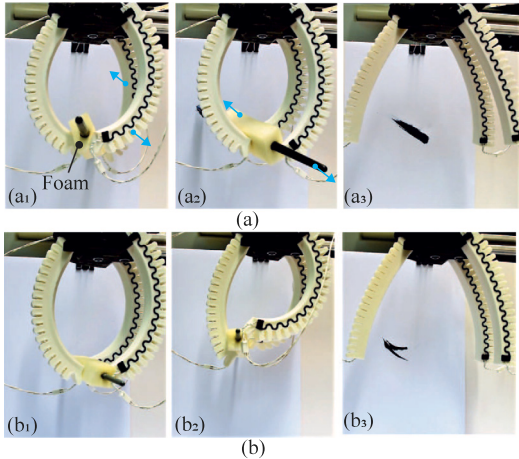


Fig. 14. Drawing process using the gripper and a painting brush. (a) The drawing of a straight line. (b) The drawing of two arcs. The subscripts 1, 2, 3 refer to the different stages of drawing. 1: hold the painting brush; 2: Drawing; 3: Release the painting brush and the painting is finished.

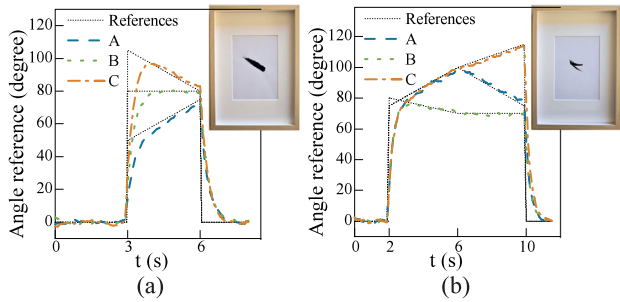


Fig. 15. The drawing results. (a) The angle references and the controlled angles for the drawing of a straight line and the mounted painting. (b) The angle references and the controlled angles for the drawing of two arcs and the mounted painting.

are identical at different stages and the stages are marked above the horizontal axis. Fig. 13(b) shows that the gripper is ready to work and the wet sponge is manually placed below the gripper. A glass Petri dish is used as the water pool to store the water. Reference angle signals are calculated from the gripper design and the sponge dimensions to enable the gripper to gently touch the sponge without pressing hard. The references are then sent to the gripper system to actuate the three actuators individually and then the gripper actuates to hold the wet soft sponge gently as shown in Fig. 13(c). In this case, the reference angles for the three actuators are 50° and there is no water leaked or squeezed out. In Fig. 13(d), larger reference signals of 75° are applied by the gripper to squeeze the wet sponge and the water is pressed out from the sponge. In the last step in Fig. 13(e), the gripper is reset to initial state and the sponge is released and falls to the water pool.

5.2. Simple drawings using painting brushes

The gripper is further applied with dynamic reference angles for each actuator to perform some simple drawings as shown in Fig. 14. A painting brush is used for the drawings and held by the gripper with the assistance of a piece of cubic shaped soft foam that covers the painting brush. Two drawings including a straight line shape and a wedge shape consisting of two arcs are performed by two kinds of gripper actuation as shown in the figures (a) and (b) respectively of Figs. 14 and 15. Fig. 14(a) shows the three steps of the drawing process of the straight line shape. The blue arrows in the figure illustrate the moving directions of the actuators and the painting brush. At step (a₁), the three actuators move towards the center to hold the painting brush.

For drawing, the reference angle for actuator A increases thus actuator A moves towards the left. Actuator C moves oppositely to the right and the shape of actuator B remains the same during drawing. As a result, the tip of the painting brush moves towards top left corner and the end of the painting brush moves towards the bottom right corner as illustrated in step (a₂). Correspondingly, the brush tip draws a straight line from the bottom right corner to the top left corner. Then the gripper is reset to the initial shape to release the painting brush and the drawing is finished as shown in step (a₃). The detailed angle reference and controlled trajectories of the actuators A, B and C are shown in Fig. 15(a). The three corresponding operation steps are marked above the horizontal axis. The right picture of Fig. 15(a) shows the mounted painting.

Fig. 14(b) shows a more complex drawing of two arcs. During the drawing process of the first arc, all actuators move to the left side. Then the painting brush moves towards the top left corner along a curve and slightly rotates around the center axis of the printing brush. For the second arc, the operations in Fig. 14(a) are repeated on the opposite direction to move the brush tip back from the top left corner to the bottom right corner. The angle reference changes for the two stage drawing and the mounted painting are shown in Fig. 15(b).

6. Conclusion

The study develops a 3D printed soft sensor that can be embedded in a soft actuator to measure its deformation angle and has negligible interference to the free deformation of the soft actuator. The sensor is printed with commercially available FDM materials, which enables convenient reproducibility by other researchers.

Printed sensors with different sine wave shapes are tested to characterize the sensor's performance in terms of the hysteresis, linearity error and drifting. The thickness and number of sine waves of the sensor are studied. The best sensor shape is then selected by evaluating the overall performance of different sensors. The best sensor is then applied to provide shape feedback using a linear sensor model for the shape estimation of the soft actuator. Compared with a commercial flexible bending sensor, the printed sensor shows less negative influences on the performance of the soft actuator and provides higher estimation accuracy with smaller standard deviation in the calibrated deformation range.

A PI controller to regulate the deformation angle of the soft actuator is developed by pole placement. The deformation angle can be measured by either the developed printed soft sensor or an accurate image processing module. Although the printed soft sensor introduces measurement errors into the controlled system, the overall control performance using the printed soft sensor is only slightly worse than the performance using the image feedback. The accuracy of the control system using the printed sensor is acceptable for general purpose applications as demonstrated in the case studies. A gripper composed of three individually controlled actuators is fabricated to perform the case studies. The test result proves the ability of the actuators to work well for both static input references and dynamic input references.

In the future, the study can be improved in the following aspects: (a) Non-linear model for the resistance-deformation relation of the sensor can be developed instead of the linear model used now. (b) The shape of the actuator can be improved so that more complex tasks can be realized such as more complex drawings and spinning a pen. (c) The gripper can be loaded on a moving stage such as a robot arm to perform automated tasks.

CRediT authorship contribution statement

Qinglei Ji: Conceptualization, Methodology, Software, Validation, Formal analysis, Investigation, Writing – original draft, Project administration. **Jakob Jansson:** Methodology, Software, Validation, Formal analysis, Investigation. **Mikael Sjöberg:** Methodology, Software, Validation, Formal analysis, Investigation. **Xi Vincent Wang:** Supervision, Writing – review & editing. **Lihui Wang:** Supervision, Writing – review & editing. **Lei Feng:** Supervision, Writing – review & editing.

Declaration of competing interest

The authors declare that they have no known competing financial interests or personal relationships that could have appeared to influence the work reported in this paper.

Data availability

Data will be made available on request

Acknowledgments

The research is financially supported by Swedish Research Council (Vetenskapsrådet) with the projects: Closed-Loop 4D Printing with High Precision, number 2017-04550, Printing of soft untethered devices with reprogrammability and self-maintainable shapes, Sweden, number 2019-05232, KTH XPRES and KTH IRIS Area 2 Integrated mechanics, Sweden, components and materials design including additive manufacturing.

Appendix A. Supplementary data

Supplementary material related to this article can be found online at <https://doi.org/10.1016/j.mechatronics.2023.102980>.

References

- [1] Ji Q, Zhang X, Chen M, Wang XV, Wang L, Feng L. Design and closed loop control of a 3D printed soft actuator. In: 2020 IEEE 16th international conference on automation science and engineering. IEEE; 2020, p. 842–8.
- [2] Liu Z, Yin X, Peng K, Wang X, Chen Q. Soft pneumatic actuators adapted in multiple environments: A novel fuzzy cascade strategy for the dynamics control with hysteresis compensation. Mechatronics 2022;84:102797.
- [3] Li Y, Liu Y, Yamazaki K, Bai M, Chen Y. Development of a soft robot-based photodynamic therapy for pancreatic cancer. IEEE/ASME Trans Mechatronics 2021.
- [4] Sitti M. Miniature soft robots—road to the clinic. Nat Rev Mater 2018;3(6):74–5.
- [5] Low JH, Khin PM, Han QQ, Yao H, Teoh YS, Zeng Y, et al. Sensorized reconfigurable soft robotic gripper system for automated food handling. IEEE/ASME Trans Mechatronics 2021.
- [6] Pilz da Cunha M, Ambergan S, Debije MG, Homburg EF, den Toonder JM, Schenning AP. A soft transporter robot fueled by light. Adv Sci 2020;7(5):1902842.
- [7] Kim Y, Yuk H, Zhao R, Chester SA, Zhao X. Printing ferromagnetic domains for untethered fast-transforming soft materials. Nature 2018;558(7709):274–9.
- [8] Elgeneidy K, Lohse N, Jackson M. Bending angle prediction and control of soft pneumatic actuators with embedded flex sensors—a data-driven approach. Mechatronics 2018;50:234–47.
- [9] Gerboni G, Diodato A, Ciuti G, Cianchetti M, Menciassi A. Feedback control of soft robot actuators via commercial flex bend sensors. IEEE/ASME Trans Mechatronics 2017;22(4):1881–8.
- [10] Cao J, Liang W, Zhu J, Ren Q. Control of a muscle-like soft actuator via a bioinspired approach. Bioinspiration Biomim 2018;13(6):066005.
- [11] Tawk C, Zhou H, Sarıyıldız E, In Het Panhuis M, Spinks GM, Alici G. Design, modeling, and control of a 3D printed monolithic soft robotic finger with embedded pneumatic sensing chambers. IEEE/ASME Trans Mechatronics 2020;26(2):876–87.
- [12] Sonar HA, Gerratt AP, Lacour SP, Paik J. Closed-loop haptic feedback control using a self-sensing soft pneumatic actuator skin. Soft Robot 2020;7(1):22–9.
- [13] Yap YL, Sing SL, Yeong WY. A review of 3D printing processes and materials for soft robotics. Rapid Prototyp J 2020.
- [14] Wallin T, Plikul J, Shepherd R. 3D printing of soft robotic systems. Nat Rev Mater 2018;3(6):84–100.
- [15] Truby RL, Wehner M, Grosskopf AK, Vogt DM, Uzel SG, Wood RJ, et al. Soft somatosensitive actuators via embedded 3D printing. Adv Mater 2018;30(15):1706383.
- [16] Elgeneidy K, Neumann G, Jackson M, Lohse N. Directly printable flexible strain sensors for bending and contact feedback of soft actuators. Front Robot AI 2018;5:2.
- [17] Hainsworth T, Smith L, Alexander S, MacCurdy R. A fabrication free, 3D printed, multi-material, self-sensing soft actuator. IEEE Robot Autom Lett 2020;5(3):4118–25.
- [18] Yang Y, Chen Y. Innovative design of embedded pressure and position sensors for soft actuators. IEEE Robot Autom Lett 2017;3(2):656–63.
- [19] Tawk C, Alici G. A review of 3D-Printable soft pneumatic actuators and sensors: Research challenges and opportunities. Adv Intell Syst 2021;2000223.
- [20] Chen M, Ji Q, Zhang X, Feng L, Wang XV, Wang L. Study on efficient fused deposition modelling of thermoplastic polyurethane inflatable wall features for airtightness. In: Swedish production symposium. 2020, JÖNKÖPING, Sweden.
- [21] Jansson J, Sjöberg M. Closed-loop control of a 3D printed soft actuator with soft position sensors. [Master's thesis], (2021:585);KTH, Mechatronics; 2021, p. 69.
- [22] Agarwala S, Goh GL, Yap YL, Goh GD, Yu H, Yeong WY, et al. Development of bendable strain sensor with embedded microchannels using 3D printing. Sensors Actuators A 2017;263:593–9.
- [23] Zolfagharian A, Kaynak A, Kouzani A. Closed-loop 4D-printed soft robots. Mater Des 2020;188:108411.
- [24] Liu M, Zhao Y, Shao Y, Zhang Q, Liu C. 3D printed force sensor with inkjet printed piezoresistive based strain gauge. In: 2018 IEEE Sensors. IEEE; 2018, p. 1–4.
- [25] Gooding J, Fields T. 3D printed strain gauge geometry and orientation for embedded sensing. In: 58th AIAA/ASCE/AHS/ASC structures, structural dynamics, and materials conference. 2017, p. 0350.
- [26] Tjur T. Coefficients of determination in logistic regression models—A new proposal: The coefficient of discrimination. Amer Statist 2009;63(4):366–72.
- [27] Tawk C, Alici G. Finite element modeling in the design process of 3D printed pneumatic soft actuators and sensors. Robotics 2020;9(3):52.
- [28] Mohamed MH, Wagdy SH, Atalla MA, Rehan Youssef A, Maged SA. A proposed soft pneumatic actuator control based on angle estimation from data-driven model. Proc Inst Mech Eng Part H: J Eng Med 2020;234(6):612–25.
- [29] Wittenmark B, Åström KJ, Årzén K-E. Computer control: An overview. IFAC Prof Brief 2002;1:2.



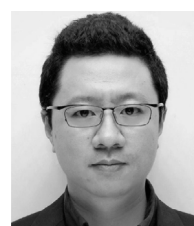
Qinglei Ji received the B.Eng. degree in Aerospace Engineering and M.Sc. degree in Engineering Mechanics from Nanjing University of Aeronautics and Astronautics, Nanjing, China, in 2015 and 2018 respectively. He also received the Diplôme d'Ingénieur in Advanced structure and M.Sc. degree in Air and ground transportation from École Nationale Supérieure de Mécanique et d'Aérotechnique, Poitiers, France in 2018. He is currently a Ph.D. student in Production Engineering with KTH Royal Institute of Technology, Stockholm, Sweden.



Jakob Jansson received the B.Sc. degree in Design and Product Realization from KTH Royal Institute of Technology, Stockholm, Sweden, in 2019. He received the M.Sc. degree in Mechatronics engineering in the same university. His research interests focus on Mechatronics systems for Life Science and Biomechanics.



Mikael Sjöberg received the B.Sc. degree in Design and Product Realization from KTH Royal Institute of Technology, Stockholm, Sweden in 2019. He received the M.Sc. in Mechatronics at the same university. His research interests focus on Mechatronics integration for Biomechanics, Life Science and Environmental engineering.



Xi (Vincent) Wang received the bachelor's degree in mechanical engineering from Tianjin University, China, in 2008, and the Ph.D. degree in mechanical engineering from The University of Auckland, New Zealand, in 2013. He is currently an Associate Professor with the IIP Department of Production Engineering, KTH Royal Institute of Technology, Sweden. He is working with the Division of Sustainable Manufacturing Systems (SPS). His main research interests include cloud-based manufacturing, sustainable manufacturing, robotics, computer-aided design, and manufacturing systems. He serves as the Managing Editor for the International Journal of Manufacturing Research (IJMR). He also serves as an Associate Editor for the SME Journal of Manufacturing Systems (JMS) and the open access journal Array (Elsevier).



Lihui Wang is a Chair Professor at KTH Royal Institute of Technology, Sweden. His research interests are focused on cyber-physical systems, real-time monitoring and control, human-robot collaborations, and adaptive manufacturing systems. Professor Wang is actively engaged in various professional activities. He is the Editor-in-Chief of International Journal of Manufacturing Research, Journal of Manufacturing Systems, and Robotics and Computer-Integrated Manufacturing. He has published 10 books and authored in excess of 550 scientific publications. Professor Wang is a Fellow of Canadian Academy of Engineering, CIRP, SME and ASME. He is also a Professional Engineer in Canada, the President (2020–2021) of North American Manufacturing Research Institution of SME, and the Chairman (2018–2020) of Swedish Production Academy.



Lei Feng received the B.S. and M.S. degrees from Xi'an Jiaotong University, Xi'an, China, in 1998 and 2001, respectively, and the Ph.D. degree from the Systems Control Group, the University of Toronto, Toronto, ON, Canada, in 2007. In 2012, he joined the Mechatronics and Embedded Control System Division, the KTH Royal Institute of Technology, Stockholm, Sweden, where he is currently an Associate Professor. His main research interests include novel mechatronic systems enabled by additive manufacturing, energy management control of mechatronic systems, autonomous driving, verification and control synthesis of cyber-physical systems, and supervisory control of discrete event systems.